GEOPHYSICS, VOL. 77, NO. 5 (SEPTEMBER-OCTOBER 2012); P. WC25–WC36, 12 FIGS., 1 TABLE.
10.1190/GEO2011-0445.1

Elastic finite-difference modeling of volcanic-hosted massive sulfide deposits: A case study from Half Mile Lake, New Brunswick, Canada

Gilles Bellefleur[1], Alireza Malehmir[2], and Christof Müller[3]

ABSTRACT

We present elastic finite-difference modeling results over a geologically realistic 2D representation of the Half Mile Lake volcanic-hosted massive sulfide deposit, New Brunswick, Canada. The model is constrained by geologic information from surface mapping and boreholes, whereas petrophysical properties are provided by wireline logging data acquired in two boreholes intersecting different parts of the deposit. We analyzed the P-P, P-S, S-P, and S-S responses of the lower and deep mineralized zones and assessed some compositional effects by substituting massive sulfides with gabbro properties in the model. Finite-difference modeling results predict complex scattering signature associated with the lower and deep sulfide zones. Both zones scattered back P-P, P-S, S-P, and S-S waves generally having strongest amplitudes in the stratigraphy down-dip direction. The P-S, S-P, and S-S scattered waves, if properly recorded on multicomponent data, represent useful signal that could help the targeting of deep sulfide mineralization. Finite-difference simulations further reveal phase-reversals on P-P wavefields scattered at the lower and deep zones. The phase reversals are not observed for gabbro inclusions, suggesting that this signature could be used to discriminate gabbro units from sulfide mineralization. The finite-difference simulation successfully reproduces many events of the VSP data, in particular P-S and S-S events on the radial component and P-P and S-P events on the vertical component. Comparison with 3D data is rather poor and only shows weak correlation with P-P events from the lower and deep zones. Despite the poor correlation, a prestack time migrated S-P section displays an amplitude anomaly at the location of the deep zone, suggesting that S-P waves were recorded on the 3D data, although this survey was acquired with explosive sources and vertical geophones.

INTRODUCTION

Volcanic-hosted massive sulfide (VHMS) deposits have a wide range of size and shape, and often combine variable proportions of economical minerals and host rocks. Such variety stems in part from the local depositional environment and subsequent tectonic history, which further explains the geologic complexity in which older VHMS deposits are typically found. In such complex environments, forward modeling techniques are commonly used to provide a better understanding of the geophysical signature of mineral deposits (Thomas et al. 2000; Cheng et al., 2006). Forward modeling techniques are also instrumental when trying to understand the key characteristics of VHMS deposits on seismic data. Hobbs (2003) used the complex-elastic screen method to model near-normal incidence VSP and surface seismic data to assess the response of the Bell-Allard VHMS deposit in Matagami, Canada. Eaton (1999) used the Born approximation to study the shape and composition effects of simple pyrite, sphalerite, and galena ellipsoid inclusions. Elastic finite-difference (FD) simulations are also well-suited to improve the understanding of wavefield scattered at VHMS deposits. L'Heureux et al. (2009) used FD simulation to study effects of heterogeneity and associated seismic scattering in mineral exploration environments and demonstrated that the scattering nature of some host rocks could reduce signal-to-noise ratio (S/N) and complicate the detection of massive sulfide deposits. Bohlen et al. (2003) used FD simulations to study the response of orebodies with various shapes and compositions embedded in a homogeneous background environment. Wavefields obtained for pure sulfide minerals (sphalerite, galena, and

Manuscript received by the Editor 3 November 2011; revised manuscript received 12 March 2012; published online 7 September 2012.
[1]Geological Survey of Canada, Ottawa, Ontario Canada. E-mail: gbellefl@nrcan-rncan.gc.ca.
[2]Uppsala University, Department of Earth Sciences, Uppsala, Sweden. E-mail: alireza.malehmir@geo.uu.se.
[3]GNS Science, Lower Hutt, New Zealand. E-mail: c.mueller@gns.cri.nz.

pyrite) were compared to those simulated for mafic rocks (gabbro) which commonly produce strong reflections when in contact with most lithologies typically found in VHMS mining camp. Results demonstrate that scattering directivity is primarily controlled by the shape of the deposit, whereas composition influences the amplitude of the scattered waves (Bohlen et al., 2003). Composition effects also include phase reversals for the first scattered arrival for sphalerite, galena, and gabbro inclusions. The scattering angle (angle between the incident wave and the direction of the scattered wave) of the phase reversal was identified as a parameter that could potentially provide information on the composition of a buried inclusion. An amplitude-versus-azimuth anomaly for a diffraction originating from a deep massive sulfide lens (known as the deep zone) at Half Mile Lake, New Brunswick, Canada, is partly considered to be the result of compositional effects (Malehmir and Bellefleur, 2009).

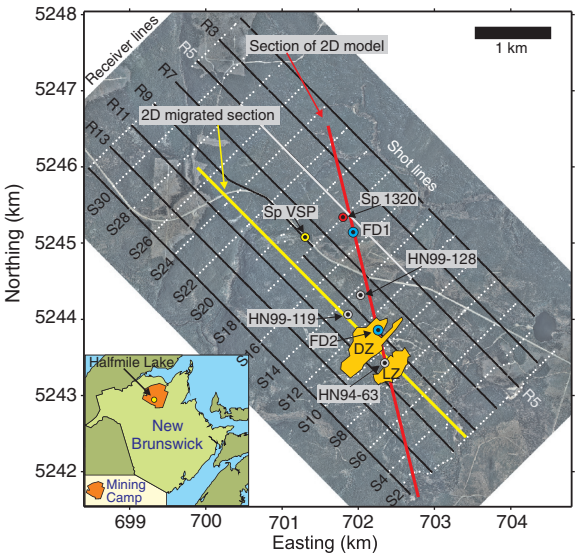

Figure 1. Acquisition geometry used for the 3D survey at Half Mile Lake. Also shown are the surface projections of the lower and deep sulphide zones (DZ and LZ). The red line shows the location of the 2D model used for the finite-difference modeling. The southeast-northwest solid yellow line indicates the location of a migrated section shown later in the paper. True dip direction of the lower and deep zones is approximately to the north. Wirleine logging data was acquired in boreholes HN99-119 and HN94-63. Borehole HN-99-128 was previously used for VSP survey. The yellow circular dot (Sp VSP) marks the shot point location of the VSP data shown also later in the paper. The blue circular dots (FD1 and FD2) show surface locations of two source locations used in the finite-difference modeling. The red circular dot (Sp 1320) is the location of a shot gather from the 3D survey discussed and shown in the paper.

Here, we use FD modeling to simulate the seismic response of a realistic 2D geologic representation of the Half Mile Lake deposit. The model is defined from a 2D geologic cross section cutting through three massive sulfide lenses (known as upper, lower, and deep zones) at the Half Mile Lake, and constrained by physical rock properties from two well-logs intersecting the mineralization. The deep zone is known for its strong amplitude response observed on 3D seismic data and its asymmetric diffraction signature (Matthews, 2002; Malehmir and Bellefleur, 2009). The purpose of the FD modeling is to further investigate the nature of the phase reversal and assess its robustness for discriminating massive sulfides from other mafic lithologies. In addition to conventional P-P reflection typically employed in mineral exploration, we also investigate the P-S, S-P, and S-S responses of the massive sulfide lenses. Such wavemodes were previously observed on VSP data from Half Mile Lake (Bellefleur et al., 2004). Finally, we compare FD results with the VSP and surface 3D data from the Half Mile Lake area. Finite-difference modeling results correlate well with VSP data and further suggest that mode-converted waves, in particular S-P waves, may have been recorded on the surface 3D seismic data, although this survey was acquired with point explosive sources (i.e., no S-wave sources) and vertical geophones.

GEOLOGIC BACKGROUND AND 2D MODEL

The Half Mile Lake VHMS deposit is located in New Brunswick, Canada, and is part of the Bathurst Mining Camp (Figure 1). The deposit consists of four zones (upper, lower, deep, and north zones) composed of pyrrhotite breccia matrix and laterally continuous layers of pyrite and pyrrhotite (Adair, 1992). The deposit is located in the Tetagouche Group, a volcano-sedimentary sequence from the Middle Ordovician (McCutcheon, 1992). The deposit has been explored since 1955, but is still undeveloped. The Half Mile Lake deposit was recently the subject of a National Instrument (NI) 43–101 compliant resource estimate (Wardrop, 2009), which estimated 6.62 Mt of indicated resources with 8.13% Zn, 2.58% Pb, 0.22% Cu, and 30.78 grams per ton (g/t) of Ag, and 6.07 Mt of inferred resources with 6.69% Zn, 1.83% Pb, 0.14% Cu, and 20.51 g/t Ag. The Half Mile Lake deposit has been tested with numerous geophysical methods, including 2D, 3D, and VSP seismic methods (Salisbury et al., 2000; Matthews, 2002; Bellefleur et al., 2004; Malehmir and Bellefleur, 2009). Most of the inferred resources identified in the NI 43–101 estimate are for the deep zone discovered with 3D seismic methods (Matthews, 2002).

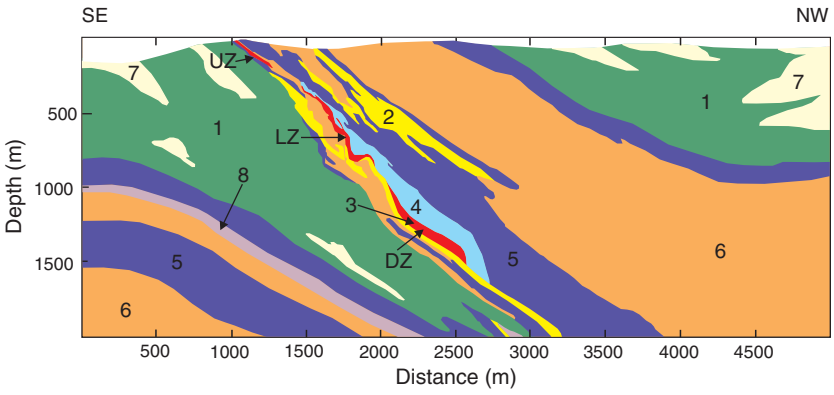

Figure 2. Composite geologic section used for the finite-difference modeling (see Figure 1 for the location). The numbers refer to lithologic units and related petrophysical properties listed in Table 1. The upper (UZ), lower (LZ), and deep (DZ) zones are also shown.

The 2D model (Figure 2) used in our FD modeling study is constrained by information obtained

from boreholes and surface geologic and geophysical mapping, and derived from an interpreted composite geologic cross section built by projecting information from nearby boreholes. In this section, the stratigraphic sequence hosting the deposit dips at approximately 45° to the north-northwest. The three mineralized zones in Figure 2 are partly deformed tabular bodies parallel to the stratigraphy. The upper zone is a thin body located close to the surface. The lower zone is particularly irregular and characterized with curvatures that are likely to scatter incident seismic waves. In comparison, the deep zone is a lightly folded and slightly thicker tabular body. The north zone, located outside of the 3D survey area shown in Figure 1, is not included in our model. The model is relatively well-constrained near the three massive sulfide lenses, but lacks geologic control elsewhere, especially at greater depths. We completed the model in those areas assuming some continuity for structures and lithologic contacts mapped at surface and in boreholes. A 3D model would have been more appropriate to investigate amplitude variation with azimuth and offset. However, such a model could not be constructed with sufficient geologic realism due to insufficient borehole coverage away from the three massive sulfide lenses.

The geologic logs used in the model construction provided a great amount of detail that could not all be taken into account and reconciled in a unique petrophysical model. As a result, detailed lithofacies information (i.e., tuff, breccia, flow for volcanic rocks or various sedimentary facies) and alterations (chlorite and sericite alterations) were not included in the model. Lithologic units with limited thickness or lateral extent, such as small dikes, were also omitted during the model construction. The model contains only sufficiently continuous rock types for which petrophysical properties could be determined.

The 2D model is a 5 km long by 2 km deep section populated every meter with P- and S-wave velocity and density. Physical properties were constrained by full waveform sonic and density logs acquired in two boreholes (HN99-119 and HN94-63; Figure 1). Detailed information on logging data for these boreholes can be found in Salisbury et al. (2000), Mwenifumbo et al. (2003), and Bellefleur et al. (2004). Table 1 presents a summary of the lithologic units of the model and their physical properties. The distribution of the physical properties for the main lithologies intersected in borehole HN99-119 is also shown in Figure 3. In general, the average values from the mineralized zones show higher density and S-wave velocity but lower P-wave velocity than host rocks intersected by the boreholes (Table 1). The standard deviations of P- and S-wave velocity of massive sulfide ore are generally high and reflect some variations in ore composition. Such variations are clearly observed for the deep zone on well-log data from borehole HN99-119 (Figure 3). Density is relatively constant, whereas velocities have high and low values related to grade variations and compositional changes (pyrite to pyrrhotite-sphalerite). The fast P- and S-wave velocities in borehole HN99-119 are generally located at the top of the deep zone whereas lower velocities are observed at the bottom of this zone (Bellefleur et al., 2004). However, detailed correlations between boreholes are not straightforward and, thus, the average petrophysical properties over the entire ore interval were used and assigned to the mineralized zones of our model. Table 1 also indicates that some lithologic contacts could produce detectable reflections, in particular when the rhyolite and quartz-feldspar porphyry (Q-F porphyry) rocks are in contact with either the sedimentary or mafic volcanic rocks.

The model shown in Figure 2 provides a realistic and controlled environment in which responses of massive sulfide lenses can be assessed. This model is referred to as "model A" in the rest of the manuscript. Model A was also used as a basis for three alternative models built to further test compositional effects. In one alternative model (referred to as model B), we substituted the physical properties of massive sulfides with those of gabbro (unit 9 in Table 1). Lithologic contacts between host rocks were removed in the two other alternative models, which comprise only the three lenses (UZ, LZ, and DZ in Figure 2) embedded in a homogeneous background. Physical properties of massive sulfides (model C) and gabbro (model D) were assigned to the lenses, whereas properties of quartz-feldspar porphyry (unit 6 in Table 1) filled the homogeneous background. The purpose of models C and D is to assess the

Table 1. Rock properties used for the Half Mile Lake 2D model. The properties are from well-logging data in boreholes HN99-119 and HN-94-63. S-wave velocities were determined from full-waveform sonic logging data in HN99-119. Mafic volcanic rocks were not intersected in this borehole. Density and P-wave velocity for this unit are from well-logs in HN-94-63 whereas V_S was estimated using a V_P/V_S ratio of 1.74. The red stripe unit is part of the model but not sampled by logging. Properties of quartz-feldspar porphyry were used in this case. Reflections from this unit because it is generally deep, should not interfere with scattering from the massive sulfides. Properties for gabbro (unit 9) are from Bohlen et al. (2003). Gabbro is used as a substitute to sulfide (unit 3) in model B and D.

Unit number	Lithology	Density (g/cm^3)	std	V_P (km/s)	std	V_S (km/s)	std	n
1	Mafic volcanics	2.69	0.075	5.800	0.171	3.330	—	43
2	Felsic volcanics	2.58	0.167	5.800	0.369	3.370	0.177	2195
3	Sulfide	3.42	0.185	5.690	0.800	3.840	0.508	347
4	Stringer zone	2.82	0.075	5.600	0.225	3.250	0.212	101
5	Sediments	2.68	0.082	5.820	0.184	3.380	0.214	4267
6	Q-F porphyry	2.46	0.081	5.830	0.277	3.350	0.156	4862
7	Rhyolite	2.58	0.167	5.800	0.369	3.370	0.177	2195
8	Red stripe	2.46	0.081	5.830	0.277	3.350	0.156	—
9	Gabbro	3.00	—	6.200	—	3.300	—	—

compositional effects and signature of the lenses without having interference of reflections from other lithologic contacts.

Elastic properties of the gabbro unit replacing sulfides in models B and D are the generic gabbro properties (Table 1) used previously by Bohlen et al. (2003). Such generic petrophysical properties were used because the two boreholes do not intersect gabbro units at Half Mile Lake. However, the presence of gabbro and other mafic lithologies is well-documented within the Bathurst Mining Camp. Gabbro and basalt rocks near the Brunswick number 6 mine located in the northeast part of the Bathurst Mining Camp have P-wave velocity ranging between 6.0 to 6.5 km/s and density ranging from 2900 to 3100 kg/m^3 (Malehmir and Bellefleur, 2010; Cheraghi et al., 2011). Thus, the generic properties used for gabbro lenses in models B and D fall within the range of values observed in well-logs in this mining camp.

We used a parallelized finite-difference method based on a second-order approximation of the time derivatives and a fourth-order approximation of the spatial derivatives solved on a staggered grid (Bohlen, 2002). The code can simulate viscoelastic behaviors, but this option was not used in the current modeling study due to the lack of attenuation properties from the study area. Our study focuses on the backscattered wavefield as only this signal might be recorded at surface or in shallow boreholes typically found in many mining camps. This approach differs from Bohlen et al. (2003) who followed a holistic approach and also analyzed signal scattered in the forward direction as well as wave phenomena occurring inside the inclusions. Responses for the VHMS zones are analyzed with time snapshots of the wavefield and synthetic seismograms, which are compared to real data examples. The separation of P- and S-waves is particularly important in the understanding of mode-conversion processes occurring at the sulfide lenses, and is achieved by applying spatial divergence and curl operators to the particle velocities. When appropriate, we also present particle velocities in the horizontal and vertical directions which provide information about the signal that could be expected on multicomponent receivers. Explosive sources placed 9 m below the surface were simulated at two shot locations (see FD1 and FD2 in Figure 1). Synthetic data were generated for VSP and surface configurations, each having a receiver separation of 5 m. The source wavelet is a Ricker signal with a center frequency of 65 Hz, similar to the dominant frequency of the Half Mile Lake 3D seismic data estimated to be between 60 and 70 Hz (Malehmir and Bellefleur, 2009).

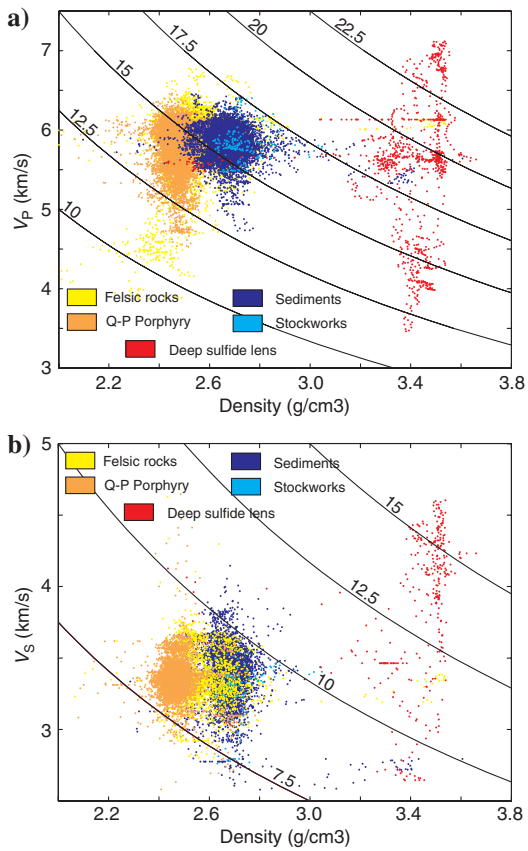

Figure 3. Density and P- and S-wave velocities derived from logging data for the main five lithologic units intersected in borehole HN99-119. P- and S-wave velocities of massive sulfides have a wide distribution indicating grade and composition variations. Lines of constant impedance (solid black lines) are also shown for reference.

FINITE-DIFFERENCE MODELING RESULTS

In this section, we show several snapshots of the wavefield, first highlighting conventional P-P waves and then other wave-modes scattered at the lower and deep sulfide zones. A snapshot of a video clip at 0.4 s showing P- and S-wavefields in model A is presented in Figure 4. The video clip (available online) provides a dynamic perspective of the various wave phenomena described in the text. Synthetic seismograms resulting from these simulations and their comparison with real data are shown in the next section.

P-P scattered waves

Figure 5 compares the compressional wavefields for the four models (A, B, C, and D) for a source located in the down-dip direction, approximately 1.3 km north of the deep zone (see FD1

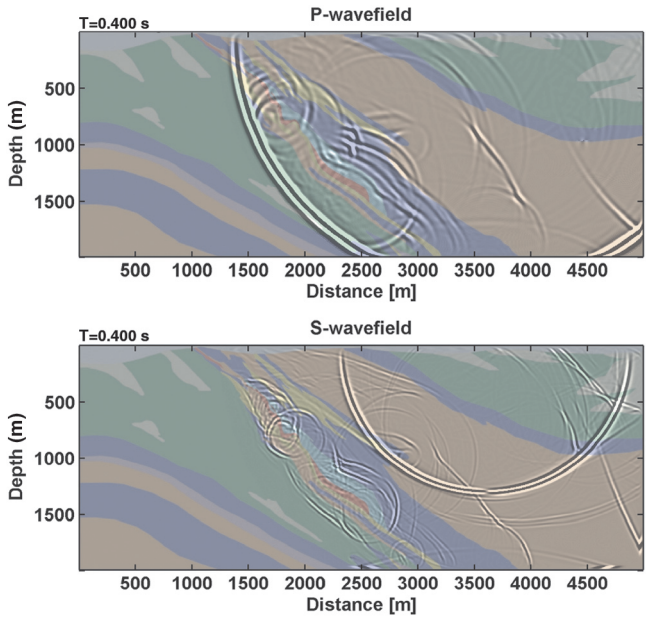

Figure 4. A snapshot of the P- and S-wavefields in model A at a time of 0.4 s. The snapshot is extracted from a video clip available online at doi: http//dx.doi.org/10.1190/geo2011-0445.2.

in Figure 1). The snapshots at 0.355 s display a combination of short but prominent reflections and scattering from the deep zone and weaker scattered waves from the deepest tip of the lower zone. Events corresponding to the top and bottom of the deep zone are observed

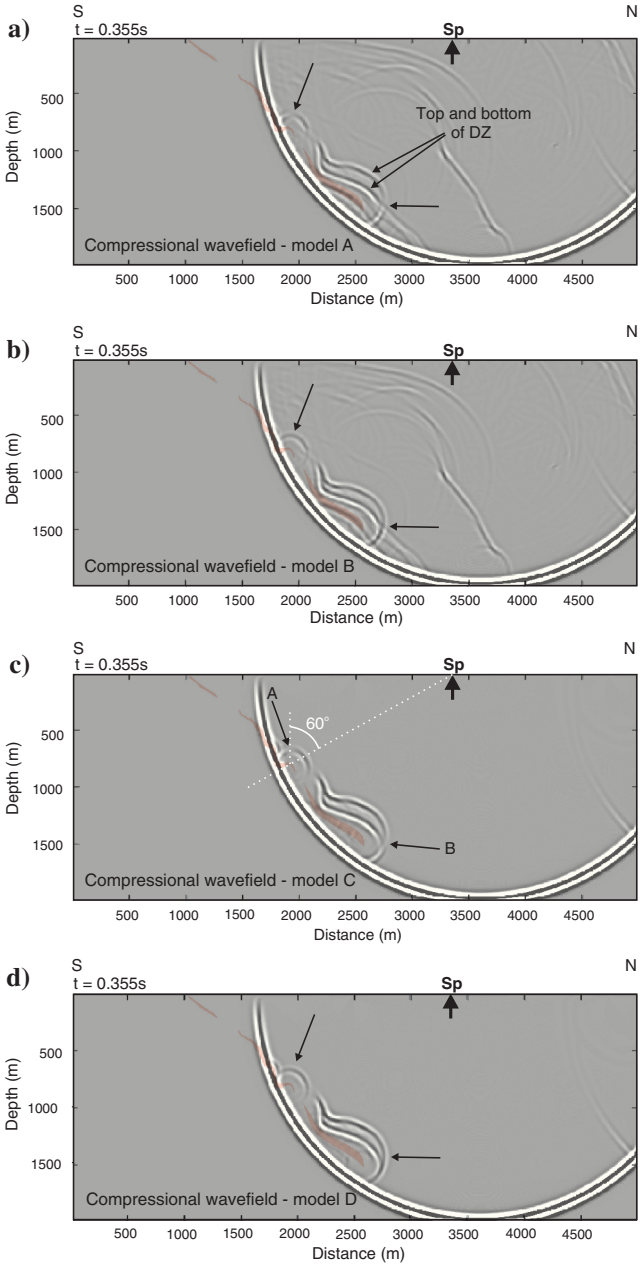

Figure 5. Snapshots of the compressional wavefield at 0.355 s for models (a) A, (b) B, (c) C, and (d) D. The shot point is located 1.3 km away from the deep zone in the down-dip direction (see FD1 in Figure 1). The main VHMS zones are shown in red in the background. Scattered P-waves from the deep zone contain strong events in the down-dip direction from the top and bottom of the massive sulfides. Scattering from the lower zone is also observed (arrow A in [c]). Arrows in (a) and (c) point to phase reversal associated with the sulfide mineralization. Such phase reversals are not observed for the gabbro models (see areas pointed by arrows in [b] and [d]). The scattering angle of the phase reversal is 60° (indicated in white in [c]). See text for the description of models A, B, C, and D.

for all models and have the strongest amplitudes in the down-dip direction. Such strong reflectivity in the down-dip direction is also a key characteristic of the deep zone on real 3D seismic data (Malehmir and Bellefleur, 2009). However, field data for the deep zone shows only one event, rather than the two shown in Figure 5 (i.e, reflections from the top and bottom of the deep zone). The difference between real and model impedances can explain this. In reality, the impedance contrasts between the lower part of the deep zone (e.g., generally characterized by lower velocities) and host rocks are slightly less than the ones in our model due to the physical rock property averaging done over the entire sulfide interval. For similar reasons, the amplitudes of the reflection from the top of the deep zone (e.g., with generally higher velocities) are likely higher, in reality, than in the FD simulations.

The wavefield for the sulfide models A and C (Figure 5a and 5c) is characterized by phase reversals identified with arrows. One phase reversal is from the lower zone (arrow A in Figure 5c) whereas the other is from the deep zone (arrow B in Figure 5c). The phase reversals are more difficult to identify on model A due to interference

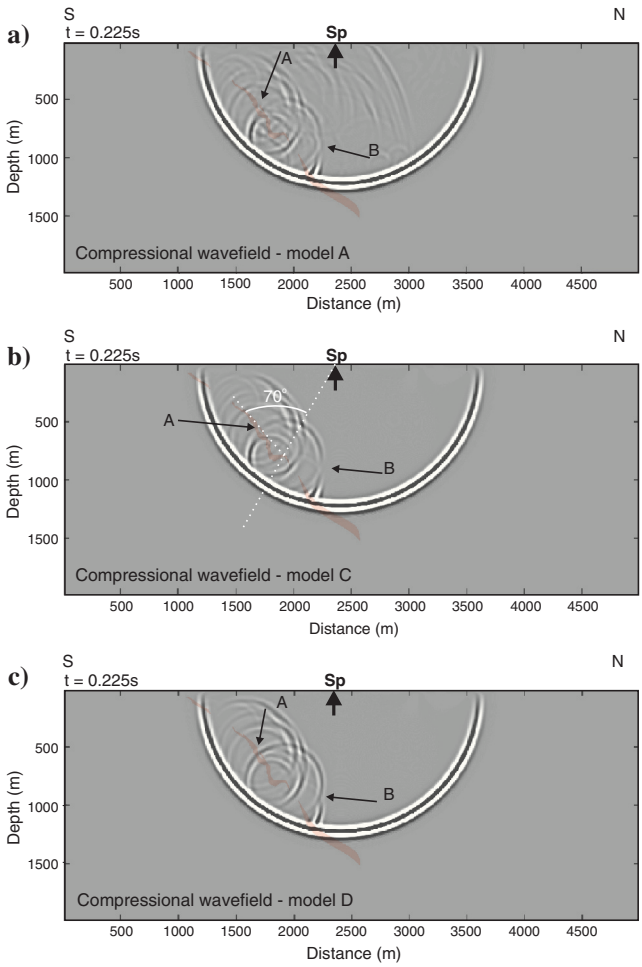

Figure 6. Snapshots of the compressional wavefields for a shot point located directly above the deep zone (see FD2 in Figure 1). Snapshots for models (a) A, (b) C, and (c) D are shown. The time of the snapshots (0.225 s) highlights the scattering response of the lower zone. Phase reversals are observed for models A and C at a scattering angle of 70°. This angle is different from the one observed on Figure 5 (60°).

with reflections originating from other lithologic contacts (Figure 5a). No phase reversal is observed on snapshots from the gabbro models B and D (Figure 5b and 5d). This suggests that phase reversals may help to discriminate massive sulfides from gabbro in this area. These results differ from those of Bohlen et al. (2003) which also showed phase reversals for inclusions of gabbroic composition. The difference is explained by the contrast of physical rock properties between the modeled inclusion and host rocks. The gabbro inclusions of Bohlen et al. (2003) have higher P- and S-wave velocity and density, than background host rocks. In our case, the same gabbro have higher P-wave velocity and density, but slightly lower S-wave velocity than rocks in the hanging-wall and footwall in model B, or than quartz-feldspar porphyry background in model D. Our study strongly suggests that compositional effects of massive sulfide and/or lithologies in specific mining areas have to be assessed in relationship with the host rock environment.

Figure 6 compares the compressional wavefields at 0.225 s for a source located almost above the deep zone (see FD2 in Figure 1) for models A, C, and D. At that time, the snapshots show the response from the lower zone. On real data, the lower zone is characterized by a weak amplitude anomaly (Malehmir and Bellefleur, 2009). In the model, the lower zone is generally thinner than the deep zone, but more importantly, highly irregular in shape and, thus, is prone to scatter incident seismic waves. The response from the lower zone is the combination of scattering occurring at irregularities and edge of the sulfide lens. The strongest scattered amplitudes are also in the down-dip direction. Similarly to snapshots in Figure 5, phase reversals are observed for the two sulfide models (model A and C) but not for the gabbro model (model D).

Comparison of the phase reversals on Figures 4 and 5 shows that the scattering angle of the phase reversal depends on the position of the shot point at surface. This is obvious when comparing the scattering angle of the phase reversal associated with the deepest concave flexure point of the lower zone. The scattering angle of the phase reversal is 60° in Figure 5c, compared to 70° in Figure 6b. The position of the shot point is the only different modeling parameter between these two figures. This suggests that phase reversals, if present on real data, will be observed at different receiver positions and, thus, might be difficult to preserve in processed images. This is particularly true for migrated images because typical algorithms ignore this effect.

P-S, S-P, and S-S scattered waves

Figure 7 shows snapshots of the compressional and shear wavefields for models C and D. The time of the snapshots were selected to emphasize the P-S, S-P, and S-S scattered energy at the deep zone. In general, the amplitudes of the waves scattered at the deep zone are larger in models A and C (i.e., sulfide models). Snapshots of the shear wavefield at 0.375 s display scattered P-S waves occurring shortly after the compressional wavefront reached the deep zone and ahead of the shear wavefront (Figure 7a and 7b). The compressional wavefield is not visible on the shear wavefield but just passed beyond the deep zone at that time. The P-S scattered waves from the ore and gabbro models have almost identical responses. Both models show a phase reversal occurring at the same scattering angle (arrows in Figure 7a and 7b). The phase reversal for this wavemode cannot be used to discriminate the composition of the inclusions. The S-P scattered waves at 0.575 s are observed on snapshots of the compressional wavefield (Figure 7c and 7d). At that time, the shear wavefront moved beyond the deep zone and S-P waves are scattered back from the sulfide lens, predominantly in the down-dip direction. The shear wavefront is not observed on the compressional-wave snapshots but can be observed in a snapshot of the shear wavefield at 0.6 s (Figure 7e). Similarly to the P-S waves, the S-P scattered waves from the ore and gabbro models show comparable responses and a phase reversal occurring at the same scattering angle. The scattered S-S waves (Figure 7e and 7f) also show similar responses for the ore and gabbro models, with a phase reversal at the same scattering angle. However, the scattering angle of the phase reversal for this wavemode is greater than for the P-S and S-P modes. Overall, the FD results indicate that phase reversal and scattering angle of the phase reversal cannot discriminate sulfide ore from gabbro on the P-S, S-P, and

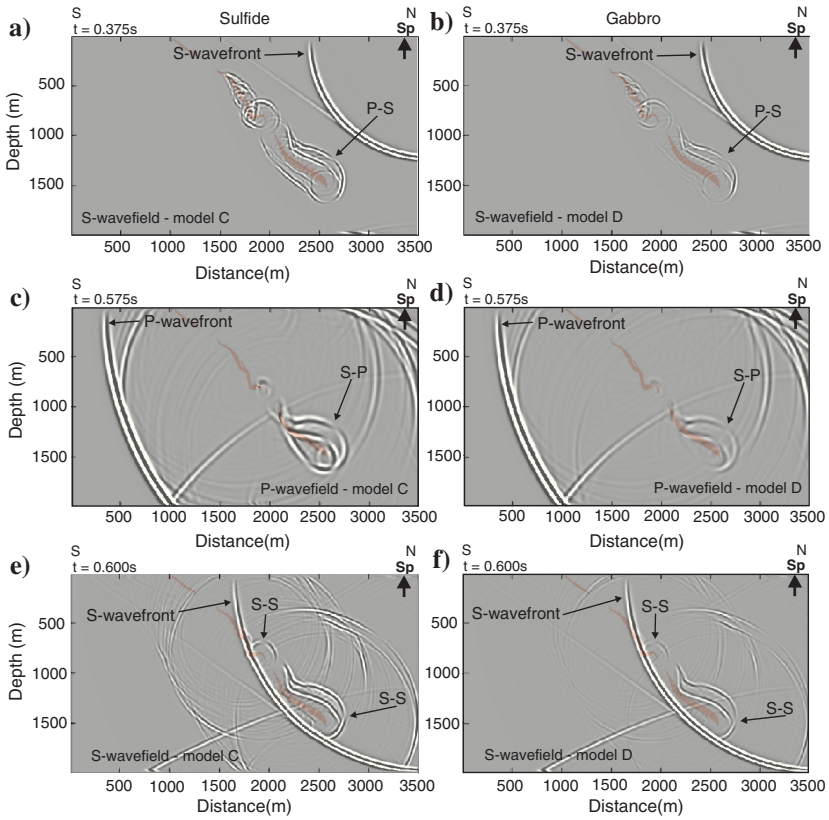

Figure 7. Snapshots of the compressional and shear-wavefield showing P-S, S-P, and S-S scattering at the deep zone for models C and D. Subfigures on the left-hand side are obtained with sulfide mineralization (model C) whereas subfigures on the right-hand side are for the gabbro model (model D). The same constant gain value was used for the display. Scattered amplitudes from the deep zone are generally stronger for the massive sulfide model (model C). Arrows point to phase reversals observed on all wave-modes. Phase reversals for model C and D show the same characteristics.

S-S modes. Thus, phase reversals might help to distinguish sulfide ore from gabbro only on scattered P-P waves.

COMPARISON WITH FIELD DATA

VSP data

Finite-difference modeling results are compared with multicomponent VSP data from Half Mile Lake (Figure 8). The multicomponent geophones of the VSP data were located in borehole HN-99-128 (Figure 1) which deviates from the vertical and intersects the deep zone at a depth of 1336 m (wireline depth). Explosives (680 g) were used at a shot point located in the down-dip direction at approximately 1.5 km north of the deep zone (see SP VSP in Figure 1). More details about the Half Mile Lake VSP data acquisition can be found in Bellefleur et al. (2004). Figure 8a shows field data after rotation into radial, transverse, and vertical components. The field data are characterized by strong downgoing P- and S-waves and significantly weaker upgoing reflections. Both Sv and Sh-waves, although not intentionally generated at the surface, are clearly observed down to the bottom of the borehole; S-waves may have been generated near the source or may result from wave conversion at the surface or at the contact between unconsolidated-consolidated layers (Lash, 1982; Edelman, 1985). The processed data (Figure 8b) displays many upgoing events previously discussed in Bellefleur et al. (2004). The annotated events (P-P, P-S, S-P, and S-S) are generated at the deep zone intersected at the bottom of borehole HN99-128. The simulated VSP data are shown in Figure 8c. Due to the 2D limitations of the model, only the particle velocities in the horizontal and vertical directions are shown. VSP data were simulated in a vertical borehole intersecting the deep zone (at the location of FD2 in Figure 1) and for a point source located approximately at 1.3 km north of the deep zone (shot point FD1 in Figure 1).

Despite slightly overestimated amplitudes for the upgoing waves, the FD simulation successfully reproduces many events of the VSP data. In particular, the downgoing P- and S-waves are well-reproduced on radial and vertical components. The FD modeling also reproduces many elements of the deep zone response observed on the processed data. Similar to the VSP data, the modeled P-S and S-S events are particularly strong on the radial component, whereas P-P and S-P events are well-defined on the vertical component. The greater continuity of the modeled upgoing waves compared with the field data may be explained by the two-dimensionality of the model. FD results also show some events originating from the lower zone (Figure 7c). However, these events are not observed on the processed VSP data. Real and modeled data confirm that P-S, S-P, and S-S events were produced at the deep zone although the VSP data was acquired with point source explosives (i.e., no S-wave source). No phase reversal is predicted by the modeling or identified on the real data for the depth range of the receivers.

Surface 3D reflection data

Figure 9 shows synthetic seismograms of the horizontal and vertical particle velocities for the sulfide ore models A and C obtained for shot point FD1 (simulated along the red line in Figure 1). Several events from the lower and deep zones are annotated. All events are stronger on the vertical component, although P-S and S-S waves have also significant amplitudes on the horizontal component. The S-S and P-S wavemodes have the polarization of shear-waves when

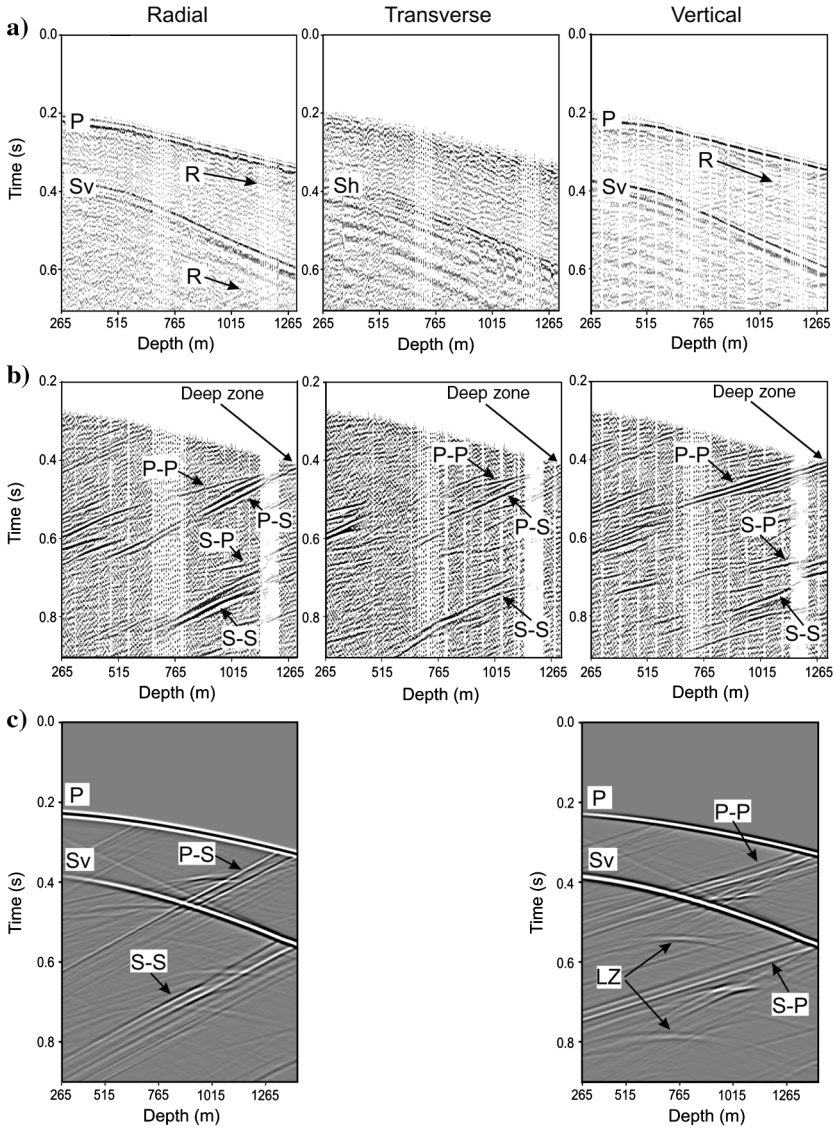

Figure 8. (a) Raw and (b) processed radial, transverse, and vertical components from a VSP data set acquired in borehole HN-99-128 (see Figure 1 for source and borehole locations). This borehole intersects the deep sulfide zone at approximately 1300 m, where strong upgoing waves are observed. Various events are annotated including P-P, P-S, S-P, and S-S waves scattered at the deep zone. The processed VSP data are modified from Bellefleur et al. (2004). The FD data (c) reproduces many of the events of the VSP data and shows scattered energy originating from the lower zone (LZ).

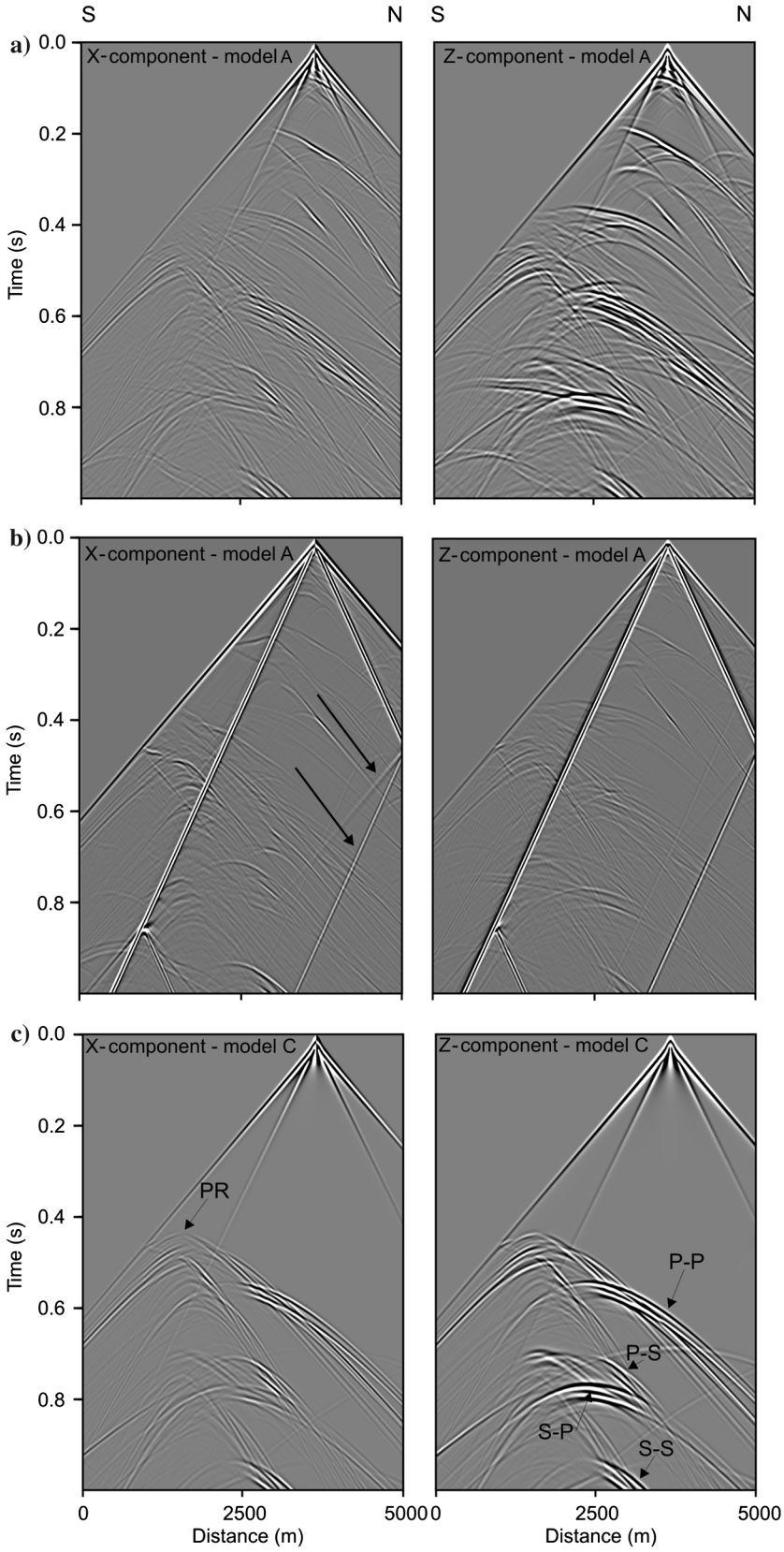

Figure 9. Synthetic seismograms for a shot located 1.3 km from the deep zone (FD 1 on Figure 1). (a) Radial and vertical components obtained for model A. Events scattered from the deep zone are more difficult to identify in due to interferences with reflections from other lithologic contacts of the model. (b) Same as (a), but modeled with a free surface. Strong Rayleigh waves ($V_R = 3075$ m/s) further mask the response of the orebody. Rayleigh waves reflected and converted at the edge of the model (arrows) are not realistic signals. (c) Radial and vertical components obtained for model C. A phase reversal clearly observed on the snapshot from model C (PR in [c]) is hard to detect in model A (a and b). The amplitude of the S-P waves scattered at the deep zone is particularly prominent on the vertical component and suggests that this wave-mode might have been recorded on the 3D field data. Display gains are different for (a-c). However, the same constant gain value was used for the display of the radial and vertical components.

they reach the surface and require multicomponent receivers to be accurately sampled over the range of offsets used in the 3D survey. The S-P waves from the deep zone are particularly prominent at relatively near offset on the vertical component, suggesting that they may have been recorded on surface data acquired with conventional vertical geophones, provided that S-waves were generated at surface. A phase reversal is observed on the synthetic seismic data from model C (PR in Figure 9c). The phase reversal can hardly be detected on the synthetic gathers from model A, due to interference with other reflections (Figure 9a). The signature of the lower and deep zones is even harder to detect when considering effects from the free surface (Figure 9b). Rayleigh waves are prominent and further mask the signal originating from the orebody.

Figure 10a shows a raw field gather (shown only for one receiver line) from the 3D surface seismic data. The 3D survey (Figure 1) covers approximately 18 km^2 with an average source and receiver line spacing of 400 m. Source and receiver intervals are 60 m and 20 m, respectively. The raw field gather in Figure 10 was acquired at shot point 1320 and contains traces along receiver line 5 between shot line 12 and 28 (Figure 1). This receiver line is at an angle of approximately 30° with the plane of the 2D model, and intersects it near shot point 1320. The 3D data were acquired with 0.5 kg explosive charge sizes placed in 9 m deep shot holes. Additional details about the 3D data acquisition can be found in Matthews (2002) and Malehmir and Bellefleur (2009). The raw field gather is characterized by strong direct and refracted P- and S-waves, surface waves, and a substantial amount of noise. Reflections are not clearly observed on the raw field gather. The same gather after basic processing is shown in Figure 10b. Processing steps included bandpass filter, deconvolution, elevation and refraction static corrections, and muting of direct and refracted P-waves, S-waves, and air blast (see Malehmir and Bellefleur [2009] for additional details on the data processing). The processed gather, although not colocated with the 2D model, lacks most of the events predicted on the synthetic data. This significant difference cannot be explained by the fact that field and modeled gathers are not exactly colocated. Two reflections located between 0.4 and 0.6 s (arrows on Figure 10b) match approximately with the modeled P-P events from the lower and deep zones. The reflections on Figure 10b are short and weak and do not indicate phase reversals. They are also observed on many shot gathers from the same area (not shown here). Other modeled events, such as the P-S, S-P, and S-S events, are not observed on the real gathers.

Discrepancies between real and modeled data suggest that imaging of the orebody using any wavemode other than the P-P waves would fail with the 3D data. We further investigated this possibility by producing a S-P prestack-time migrated section (Figure 11). The S-P wavemode was chosen because FD results predicted a strong response on vertical geophones. In addition, downgoing waves on the VSP data clearly show shear wave energy reaching the deep zone. The migrated image is produced with a 3D diffraction stack algorithm (Miller et al., 1987) modified for S-P wave-modes following an approach described in Malehmir et al. (2010). The travel path between the source and a point in the image space is separated from the trajectory between that point and a receiver at surface. Different velocities are assigned to each trajectory during the migration process, allowing the imaging of any wavemodes. Thus, the S-P image is produced by using S-wave velocity for the travel path between the source and the image point, whereas P-wave velocity is used for the trajectory between the image point and the receiver. The preferential P-wave scattering directivity identified by Malehmir and Bellefleur (2009) also suggests searching for strong seismic scattering in the down-dip direction. Thus, the migrated image in Figure 11 is generated by using source and receiver located in the down-dip direction relative to the image point in the subsurface. The P-S amplitude anomaly (Figure 11a) is found at the same location as the P-P anomaly from the deep zone (Figure 11b). The P-S amplitude anomaly is best focused when using a constant P-wave velocity of 5700 m/s and constant S-wave velocity of 3250 m/s, but the anomaly is still observed with S-wave velocities ranging from 3100 to 3400 m/s. A P-wave velocity of 5700 m/s is consistent with velocities obtained during velocity analysis of the 3D data (Malehmir and Bellefleur, 2009). The amplitude anomaly, although weak, suggests that S-P waves originating from the deep zone were recorded on the 3D data acquired with explosives (i.e., no S-wave source) and vertical geophones.

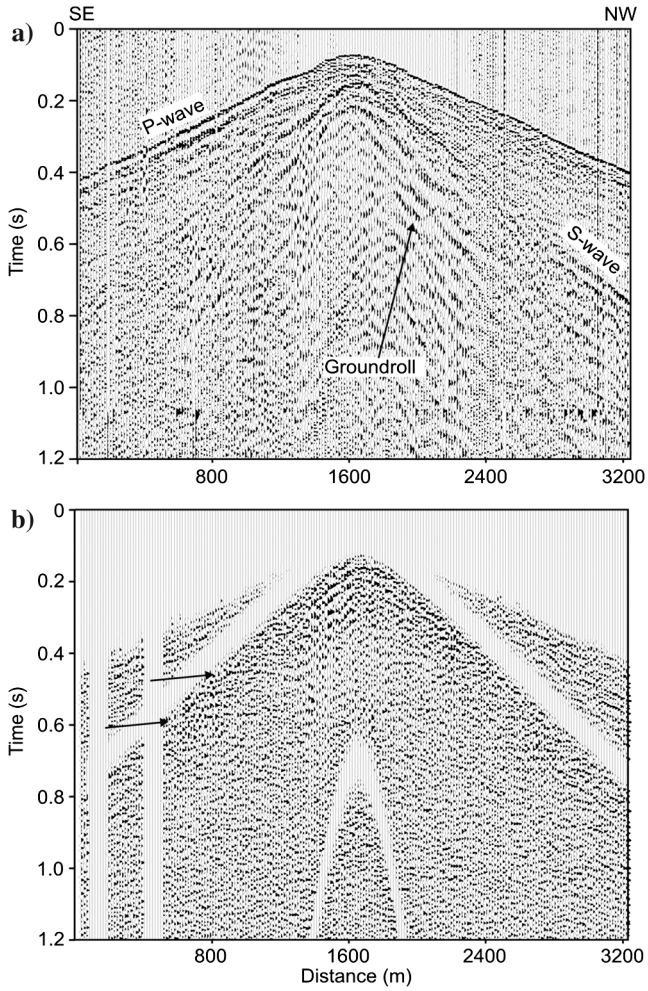

Figure 10. (a) Raw and (b) processed versions of shot gather 1320 (see Figure 1 for location). Data from receiver line 5 is shown (see Figure 1 for location of this line). The raw shot gather does not reveal any reflection. The processed data shows two reflections indicated by arrows that may correspond to the modeled P-P events from the lower zone (see Figure 9).

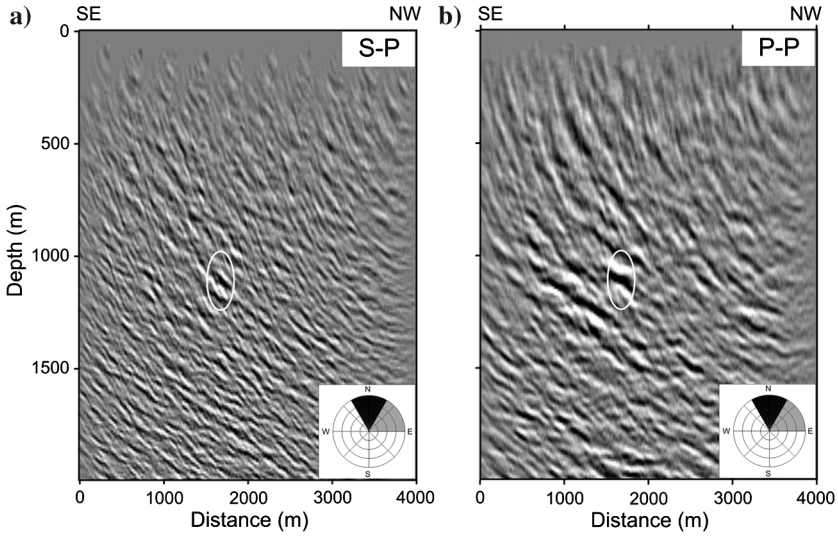

Figure 11. (a) S-P and (b) P-P prestack-time migration section intersecting the deep zone (see Figure 1 for the location of the section). The S-P migrated section is obtained following a procedure described in Malehmir et al. (2010) using constant P- and S-wave velocity of 5700 m/s and 3250 m/s, respectively. The P-P migrated section used a constant velocity of 5700 m/s. Only shot points located north of the subsurface image points were used in the migration (indicated by the black sector in the compass insert) whereas azimuth of receivers relative to the image point are indicated by the gray sector. Sources and receivers are approximately in the stratigraphy down-dip direction. An amplitude anomaly is observed on S-P and P-P images at the position of the deep zone (indicated with an ellipse).

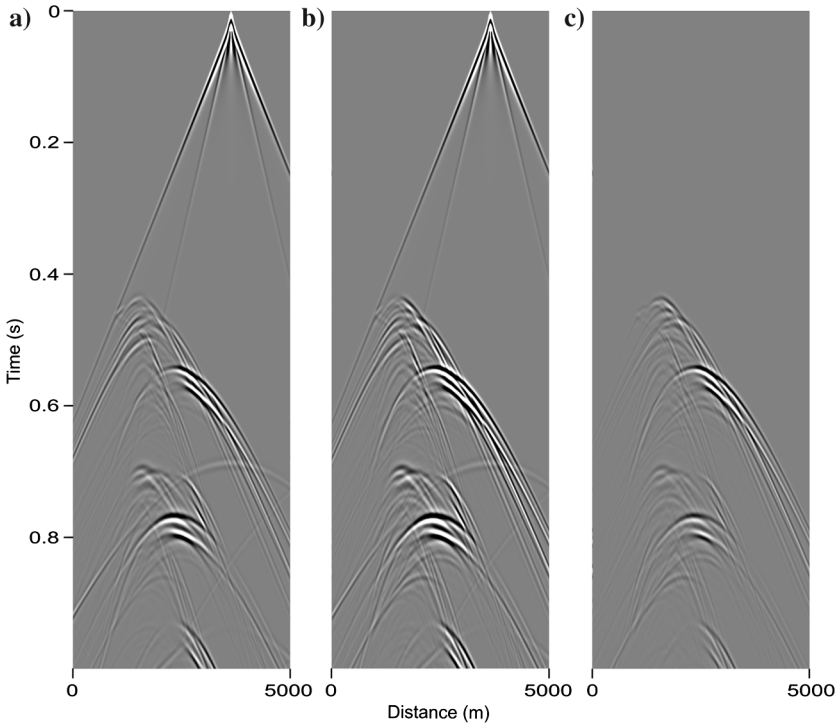

Figure 12. (a) Vertical component of a synthetic shot gather over massive sulfides (model C) using a density of 3.42 g/cm^3. (b) Same as (a), but with a density of 4.5 g/cm^3. (c) Difference between (b) and (a) (b minus a). A higher density value increases the amplitudes but does not change the kinematics of the response. Same display gain has been applied to (a–c).

DISCUSSION

Petrophysical values from well-logging data were used to obtain model parameters based on a large number of measurements, to ensure that each lithology is statistically represented. However, many density values for massive sulfides shown in Figure 3 appear clipped at approximately 3.5 g/cm^3, indicating that higher density values are expected for those measurements. Density measurements derived from gamma-gamma logging tools used at Half Mile Lake saturate at approximately 3.5 g/cm^3, because the ratio of atomic number to atomic weight (Z/A) becomes nonlinear for sulfide minerals with atomic numbers greater than 20 (Mwenifumbo et al., 2005). The nonlinear Z/A ratio invalidates standard density calibration procedures and produces underestimated density values. In addition, photoelectric absorption becomes significant in the presence of heavier elements such as galena, and significantly perturbs the count rate assumed to result from Compton scattering (Mwenifumbo et al., 2005). Unfortunately, there are no easy ways of finding the unclipped values of those density measurements. We generated synthetic data using a more realistic density value of 4.5 g/cm^3 for massive sulfides (Salisbury et al., 2000; Malehmir et al., 2012) to confirm that the data and wavefields shown above are still realistic. Figure 12 presents a comparison of synthetic data generated for model C using densities of 3.5 g/cm^3 and 4.5 g/cm^3 for the massive sulfide lenses. Both density values produce the same kinematic response, but stronger amplitudes are observed for the higher density value. Thus, results presented in the paper slightly underestimate the amplitude response of the massive sulfide orebody.

The comparison between the FD results and the VSP data is helpful and shows an excellent correlation between the modeled and observed events originating from the deep zone. Such correlation confirms that the model is adequate and provides a realistic response of the orebody. However, the poor correlation between the FD results and the 3D seismic data raises some questions. There are some differences between VSP and the surface 3D data that could explain the discrepancies. First, surface waves which are sometimes significant on surface 3D data are generally not a problem on VSP data. Surface waves represent additional noise requiring special attention during processing. Second, the travel path from a source to a scatterer to a receiver is generally much larger for the 3D survey. As a result, effects from attenuation will be more important and S/N will be much lower on the 3D data. Effects of scattering due to heterogeneity (L'Heureux et al., 2009) are generally more significant for larger travel

path. No study confirms the intensity or significance of these two phenomena in the Half Mile Lake area. However, they are common enough in hard rock environments (Frankel and Clayton, 1986; Frankel, 1991; Holliger and Goff, 2003) that we can presume they affected the 3D data. Attenuation and heterogeneity likely affected the VSP data, but their impact was not as significant as on the 3D data due to the shorter travel path (VSP receivers were very close to the massive sulfide mineralization). Thus, we suggest that surface waves, attenuation, and scattering combined with the generally longer travel path of the 3D data may partly explain the poor correlation between the FD results and the 3D data.

The FD modeling results clearly indicate that nonconventional wavemodes (P-S, S-P, and S-S) could help in the targeting of deep sulfide mineralization. However, before they can be used for that purpose, P-S, S-P, and S-S waves scattered at a mineralized body first require data acquisition enabling the recording of the full wavefield with multicomponent receivers and P- and S-wave sources. Up to now, only a limited number of multicomponent surveys were acquired for mineral exploration (Snyder et al., 2008; Malinowski and White, 2011) whereas no surveys have been acquired with S-wave sources. Such surveys are required to fully understand the main acquisition, processing, and imaging challenges associated with nonconventional wavemodes and their real benefits for mineral exploration.

CONCLUSIONS

Finite-difference modeling over a geologically realistic representation of the Half Mile Lake VHMS deposit predicts complex scattering signatures associated with the lower and deep sulfide zones. Both zones scatter back P-P, P-S, S-P, and S-S waves and generally show strongest amplitudes in the down-dip direction. The P-S, S-P, and S-S scattered waves, if properly recorded on multicomponent data, represent useful signals that could help targeting deep sulfide mineralization.

Finite-difference simulations reveal phase-reversals on P-P wavefields scattered at the lower and deep zones. The phase reversals are not observed for gabbro inclusions, suggesting that this signature could be used to discriminate gabbro units from sulfide mineralization in the Bathurst Mining Camp. Phase reversals are also observed on P-S, S-P, and S-S wavefields scattered at the deep zone, but those exhibit the same characteristics for gabbro and sulfide composition. This suggests that phase reversals for these wavemodes are of geometric origin. Although feasible with FD results, the discrimination of sulfide ore and gabbro inclusions with P-P phase reversal will likely be challenging on real data. Interferences with other reflections and the generally high noise level often observed in mining camps will complicate the recognition and preservation of the subtle characteristics of this signature during processing.

The FD simulation realistically reproduces many events associated with the deep zone on the VSP data; in particular, P-S and S-S events on the radial component, and P-P and S-P events on the vertical component. Comparison with 3D data is rather poor and only shows weak correlation for P-P events possibly related to the lower and deep zones. Despite the poor correlation, a prestack time migrated S-P section displays an amplitude anomaly at the location of the deep zone, suggesting that S-P waves were recorded on the 3D data, although this survey was acquired with explosive sources and vertical geophones. These encouraging results further indicate that multicomponent surveys are required to fully understand the main acquisition, processing, and imaging challenges associated with nonconventional wavemodes and their real benefits for mineral exploration.

ACKNOWLEDGMENTS

We thank Larry Matthews for earlier discussions on the seismic work in the Bathurst mining camp. Xstrata Zinc is acknowledged for providing access to seismic and support data, and for permission to release these results. Special thanks to T. Bohlen for providing the finite-difference modeling code used in this study. Comments from B. Milkereit, N. Stolz, and T. Bohlen improved an earlier version of the paper. The authors thank P. Hatherly, M. Salisbury, M. Urosevic, I. Vasconcelos, and one anonymous reviewer for their comments and suggestions which improved this manuscript. G. B. thanks Barbara Dietiker for her help in generating the multimedia video clip. Part of the data processing was done with Globe Claritas™. This is Geological Survey of Canada contribution 20110270.

REFERENCES

Adair, R. N., 1992, Stratigraphy, structure, and geochemistry of the Half Mile Lake massive-sulfide deposit, New Brunswick: Exploration and Mining Geology, **1**, 151–166.

Bellefleur, G., C. Müller, D. Snyder, and L. Matthews, 2004, Downhole seismic imaging of a massive sulfide orebody with mode-converted waves, Half Mile Lake, New Brunswick, Canada: Geophysics, **69**, 318–329, doi: 10.1190/1.1707051.

Bohlen, T., 2002, Parallel 3D viscoelastic finite difference seismic modelling: Computers & Geosciences, **28**, 887–899, doi: 10.1016/S0098-3004(02)00006-7.

Bohlen, T., C. Müller, and B. Milkereit, 2003, Elastic wave scattering from massive sulfide orebodies: On the role of composition and shape, *in* B. Milkereit, D. Eaton, and M. Salisbury, eds., Hardrock seismic exploration: SEG, 70–89.

Cheng, L. Z., R. S. Smith, M. Allard, P. Keating, M. Chouteau, J. Lemieux, A. Vallée, D. Bois, and D. K. Fountain, 2006, Geophysical case study of the Iso and New Insco deposits, Québec, Canada: Part II: Modeling and interpretation: Exploration and Mining Geology, **15**, 65–74, doi: 10.2113/gsemg.15.1-2.65.

Cheraghi, S., A. Malehmir, and G. Bellefleur, 2011, 2D seismic reflection imaging in the Brunswick no. 6 massive sulphide and iron deposits, Bathurst Mining Camp, Canada: Implications for crustal architecture and mineral potential: Tectonophysics, **506**, 55–72, doi: 10.1016/j.tecto.2011.04.011.

Eaton, D., 1999, Weak elastic scattering from massive sulfide orebodies: Geophysics, **64**, 289–299, doi: 10.1190/1.1444525.

Edelmann, H. A. K., 1985, Shear-wave energy source, *in* G. Dohr, ed., Seismic shear waves, Part B: Applications: Geophysical Press, 134–177.

Frankel, A., 1991, Mechanisms of seismic attenuation in the crust: Scattering and anelasticity in New York state, South Africa, and Southern California: Journal of Geophysical Research, **96**, 6269–6289, doi: 10.1029/91JB00192.

Frankel, A., and R. W. Clayton, 1986, Finite-difference simulations of seismic scattering: Implications for the propagation of short-period seismic waves in the crust and models of crustal heterogeneity: Journal of Geophysical Research, **91**, 6465–6489, doi: 10.1029/JB091iB06p06465.

Hobbs, R. W., 2003, 3D modeling of seismic-wave propagation using complex elastic screens, with application to mineral exploration, *in* B. Milkereit, D. Eaton, and M. Salisbury, eds., Hardrock seismic exploration: SEG, 59–69.

Holliger, K., and J. Goff, 2003, A generic model for the 1/f-nature of seismic velocity fluctuations in heterogeneity in the crust and upper mantle, *in* J. A. Goff, and K. Holliger, eds., Nature, scaling, and seismic properties: Kluwer Academic/Plenum Publishers, 131–154.

Lash, C. C., 1982, Investigation of multiple reflections and wave conversion by means of a vertical wave test (vertical seismic profiling) in southern Mississippi: Geophysics, **47**, 977–1000, doi: 10.1190/1.1441376.

L'Heureux, E., B. Milkereit, and K. Vasudevan, 2009, Heterogeneity and seismic scattering in exploration environments: Tectonophysics, **472**, 264–272, doi: 10.1016/j.tecto.2008.04.001.

Malehmir, A., M. Andersson, M. Lebedev, M. Urosevic, and V. Mikhaltsevitch, 2012, Experimental estimation of velocities and anisotropy of a series of Swedish crystalline rocks and ores: Geophysical Prospecting, **60**.

Malehmir, A., and G. Bellefleur, 2009, 3D seismic reflection imaging of volcanic-hosted massive sulfide deposits: Insights from reprocessing of the Half Mile Lake data, New Brunswick, Canada: Geophysics, **74**, no. 6, B209–B219, doi: 10.1190/1.3230495.

Malehmir, A., and G. Bellefleur, 2010, Reflection seismic imaging and physical properties of base-metal and associated iron deposits in the Bathurst Mining Camp, New Brunswick, Canada: Ore Geology Review, **38**, 319–333, doi: 10.1016/j.oregeorev.2010.08.002.

Malehmir, A., G. Bellefleur, and C. Müller, 2010, 3D diffraction and mode-converted scattering signatures of base-metal deposits, Bathurst mining camp, Canada: First Break, **28**, 41–45.

Malinowski, M., and D. White, 2011, Converted wave seismic imaging in the Flin Flon mining camp: Journal of Applied Geophysics, **75**, 719–730. doi: 10.1016/j.jappgeo.2011.09.026.

Matthews, L., 2002, Base metal exploration: Looking deeper and adding value with seismic data: CSEG Recorder, **27**, 37–43.

McCutcheon, S. R., 1992, Base-metal deposits of the Bathurst-Newcastle district: Characteristics and depositional models: Exploration and Mining Geology, **1**, 105–119.

Miller, D., M. Oristaglio, and G. Beylkin, 1987, A new slant on seismic imaging: Migration and integral geometry: Geophysics, **52**, 943–964, doi: 10.1190/1.1442364.

Mwenifumbo, C. J., M. Salisbury, B. E. Elliott, and K. A. Pflug, 2005, Use of multichannel gamma-gamma logs to improve the accuracy of log-derived densities of massive sulfides: Petrophysics, **46**, 346–353.

Mwenifumbo, J., B. E. Elliott, and P. Street, 2003, Massive sulphide deposits of the Bathurst mining camp, New Brunswick, and northern Maine, *in* W. D. Goodfellow, S. R. McCutcheon, and J. M. Peter, eds., Economic Geology Monograph 11, 841–860.

Salisbury, M., B. Milkereit, G. Ascough, R. Adair, L. Matthews, D. R. Schmitt, J. Mwenifumbo, D. W. Eaton, and J. Wu, 2000, Physical properties and seismic imaging of massive sulfides: Geophysics, **65**, 1882–1889, doi: 10.1190/1.1444872.

Snyder, D. B., P. Cary, and M. Salisbury, 2008, 2D-3C high-resolution seismic data from the Abitibi Greenstone Belt, Canada: Tectonophysics.

Thomas, M. D., J. A. Walker, P. Keating, R. Shives, F. Kiss, and W. D. Goodfellow, 2000, Geophysical atlas of massive sulphide signatures, Bathurst mining camp, New Brunswick: Geological Survey of Canada Open File 3887.

Wardrop, 2009, Half Mile Lake Technical Report and Resource Estimate: NI 43-101 compliant technical report to Beartooth Platinum Corp., Document number 0887190200-REP-L0002-02, p. 89, http://www.trevaliresources.com/i/pdf/Halfmile_Lake_Tech_Report_Resource_Estimate_Feb_17_2009.pdf, accessed September 9, 2011.